Research Square

Preprints are preliminary reports that have not undergone peer review.
They should not be considered conclusive, used to inform clinical practice,
or referenced by the media as validated information.

Graphene Nanoribbon Sensors for Prosthetic Socket Wear-Time Monitoring: A Lambert W Function Framework

Farrukh A. Chishtie

fachisht@uwo.ca

University of British Columbia

Mona Alkhudair

University of British Columbia

Abdullah Alsuriby

University of British Columbia

William C. Miller

University of British Columbia

W. Ben Mortenson

University of British Columbia

Article

Keywords:

Posted Date: November 3rd, 2026

DOI: https://doi.org/10.21203/rs.3.rs-11354193/v1

License: This work is licensed under a Creative Commons Attribution 4.0 International License.
Read Full License

Additional Declarations: No competing interests reported.

Graphene Nanoribbon Sensors for Prosthetic Socket Wear-Time Monitoring: A Lambert W Function Framework

Farrukh A. Chishtie[1,2,*], Mona Alkhudair[3,4,5], Abdullah Alsuriby[3], William C. Miller[2,3,] & W. Ben Mortenson[2,3,4,6]

[1]Peaceful Society, Science and Innovation Foundation, Vancouver, British Columbia, Canada
[2]Department of Occupational Science and Occupational Therapy, The University of British Columbia, Vancouver, British Columbia, Canada
[3]Graduate Program in Rehabilitation Sciences, The University of British Columbia, Vancouver, British Columbia, Canada
[4]Centre for Aging SMART Rehabilitation Research Program, GF Strong, Vancouver Coastal Health Research Institute, Vancouver, British Columbia, Canada
[5]Department of Occupational Therapy, The King Saud Bin Abdulaziz University for Health Sciences, Riyadh, Saudi Arabia
[6]International Collaboration on Repair Discoveries (ICORD), Vancouver, British Columbia, Canada

[*]Corresponding author. E-mail: fachisht@uwo.ca

Abstract

Objective measurement of prosthetic socket use, encompassing wear time together with the pressures, strains, and microclimate at the limb–socket interface, would strengthen prosthetic rehabilitation research by complementing self-report measures, which are prone to recall error and social desirability bias. Existing thermal wear-time sensors face a fundamental limitation inside prosthetic sockets: the silicone liner worn over the residual limb attenuates body heat, and in the Limbkit study of 3D-printed sockets a validated commercial temperature microsensor consequently recorded zero wear time despite reported daily use of 11 h to 15 h. Here we present a theoretical framework based on graphene nanoribbon (GNR) quantum sensors that addresses this limitation through the Lambert W function branch-point enhancement mechanism, with sensitivity scaling as $\eta_{\mathrm{enh}} \propto \delta^{-1/2}$ near $z = -1/e$ and 35-fold amplification at $\delta = 0.001$. Combining this enhancement with a steady-state heat transfer model of the residual limb–liner–socket–sensor system, we show theoretically that enhanced GNR sensors can resolve the 3 °C to 5 °C liner-attenuated differentials with millikelvin-scale noise-equivalent temperature differences, and that instrumenting the liner itself removes the thermal barrier entirely. A multi-modal architecture sensing temperature, pressure, strain, and humidity provides redundant wear classification and a route toward monitoring skin health at the interface.

Keywords: prosthetic socket, wear-time monitoring, graphene nanoribbon, quantum sensor, Lambert W function, wearable sensors, 3D-printed prosthesis, rehabilitation technology, adherence measurement, multi-modal sensing, skin–device interface

1 Introduction

Prosthetic rehabilitation following lower limb amputation depends critically on the duration and consistency of prosthetic use, as functional outcomes, gait stability, and long-term health are closely correlated with daily wear time [1, 2]. Objective measurement of socket use serves several distinct purposes. Because self-reported wear-time data are subject to recall error and social desirability bias, and can overestimate adherence by 20 % to 40 % compared with objective measures [3], sensor-based measurement offers a way to understand wearing tolerance trends over the course of rehabilitation, to serve as a proxy for recovery trajectories, to document the necessity and utilisation of devices for funders, and more broadly to inform our understanding of prosthesis-related outcomes. Objective use data also provide essential context for interpreting functional measures such as step counts, since changes in performance may reflect variation in adherence rather than differences in prosthetic performance. Sensor data of this kind complement rather than replace self-report: a sensor can establish when the prosthesis was worn, for how long, and where loading occurred, whereas only the wearer can say why it was or was not worn, whether wearing was comfortable or painful, whether it interfered with participation, or whether a period of non-wear reflected a meaningful choice. Both kinds of information are needed to interpret wearing behaviour in clinical practice and research, a point we return to in Section 7.

Wear time, however, is only one of the quantities of clinical interest at the limb–socket interface. The pressures and strains transmitted between the residual limb and the socket wall are directly implicated in skin breakdown, a major complication of prosthetic use, as are the temperature and humidity of the skin microclimate inside the liner, and continuous interface monitoring is a recognised gap across skin–device interfaces more generally. Existing pressure-mapping technologies, such as those used for wheelchair cushions, suffer from creep and hysteresis that limit their accuracy in prolonged use [4]. A sensing platform that measures temperature, pressure, strain, and moisture simultaneously, stably, and within the socket itself would therefore address both the adherence measurement problem and the broader interface health problem. The framework developed in this paper is constructed with this multi-parameter goal in view.

The Orthotimer (Rollerwerk Medical, Balingen, Germany) is a commercial temperature-based microsensor system ($9 \times 13 \times 4.5\,\mathrm{mm}$) originally developed for monitoring adherence to orthopedic devices including scoliosis braces, diabetic footwear, and foot orthoses [3, 5, 6]. The system operates by recording temperature at regular intervals; when the sensor detects temperatures within the body-heat range of 29 °C to 38.5 °C, the device is classified as being worn. Validation studies for footwear applications have demonstrated excellent correlation ($r = 0.995$) between sensor-based and camera-based wear-time measurements when appropriate temperature-classification algorithms are employed [3].

However, the prosthetic socket environment presents a fundamentally different thermal landscape from the orthotic applications for which the Orthotimer was designed. In a pros-

thetic socket, particularly those fabricated using 3D printing with polyethylene terephthalate glycol (PETG) filament, the residual limb is encased in a silicone liner of 3 mm to 6 mm thickness before insertion into the socket [7]. This liner serves essential biomechanical functions, distributing pressure, reducing shear stress, and providing cushioning, but simultaneously acts as a thermal insulator between the body surface and any temperature sensor embedded in the socket wall. The thermal conductivity of medical-grade silicone ($k_{\text{silicone}} \approx 0.2\,\text{W}\,\text{m}^{-1}\,\text{K}^{-1}$) is substantially lower than that of skin ($k_{\text{skin}} \approx 0.5\,\text{W}\,\text{m}^{-1}\,\text{K}^{-1}$), creating a temperature gradient that, under realistic ambient and metabolic conditions, can reduce the sensor-side temperature below the 29 °C detection threshold [8].

This limitation was encountered directly during the Limbkit study, a mixed-methods AB single-subject research design evaluating 3D-printed PETG prosthetic sockets in individuals with lower limb amputation, with preliminary results presented at the ISPO 20th World Congress [9, 10]. Ten participants were recruited (eight completed both phases), and adherence was monitored with an Orthotimer temperature microsensor deployed in each socket. The fabrication workflow and functional-mobility outcomes are reported elsewhere [9, 10]; here we report only the wear-time observations. Despite successful deployment of ten Orthotimer sensors, the recorded data showed systematic zero-hour wear times across entire monitoring periods, even though participants reported daily prosthetic use of 11 h to 15 h in self-report logs. The discrepancy is attributable to the liner-induced thermal attenuation rendering the Orthotimer's fixed temperature threshold ineffective for the prosthetic socket geometry. To our knowledge, no published literature has reported the use of the Orthotimer or equivalent thermal sensors specifically within prosthetic sockets, representing both a critical knowledge gap and an unmet technological need.

In this paper, we propose a fundamentally different approach to prosthetic socket use monitoring based on graphene nanoribbon (GNR) quantum sensors. Graphene, a two-dimensional carbon allotrope with extraordinary electronic, thermal, and mechanical properties, has emerged as a transformative platform for sensing applications across biomedical, environmental, and physical domains [11–13]. The charge carriers in graphene behave as massless Dirac fermions with a Fermi velocity $v_F \approx 10^6\,\text{m}\,\text{s}^{-1}$, rendering the material exquisitely sensitive to external perturbations including temperature, pressure, strain, and chemical environment [14, 15].

The theoretical framework developed here is grounded in the Lambert W function, which provides exact analytical solutions to the transcendental equations governing quantum confinement in GNRs [15, 16]. The Lambert W function, defined as the inverse of $f(W) = We^W$, exhibits a branch-point singularity at $z = -1/e$ where its derivative diverges, providing a mathematical mechanism for systematic sensitivity enhancement. This framework was recently established and comprehensively verified in a companion paper [15], which demonstrated a universal sensitivity factorization across biomedical, environmental, and physical sensing modalities. By engineering GNR sensor parameters such that the operating point lies near this singularity, enhancement factors of 35-fold and beyond can be achieved, enabling detection of attenuated thermal signals that conventional thermistors with fixed thresholds cannot resolve through prosthetic liner barriers. Figure 1 summarises both the thermal barrier problem and the proposed transduction chain.

The paper is organized as follows. Section 2 reviews current methods for monitoring prosthetic socket use, their limitations, and the relevant properties of graphene-based sensors.

Section 3 presents a quantitative analysis of the thermal barrier problem in prosthetic sockets. Section 4 develops the Lambert W enhanced temperature sensing framework and derives minimum detectable temperature differentials through liner barriers. Section 5 extends the framework to multi-modal sensing, including a moisture channel for skin-health monitoring. Section 6 discusses practical integration with 3D-printed PETG sockets and the choice of sensor placement within the socket–liner system. Section 7 addresses clinical implications, the interpretation of wear-time data, user experience and acceptability, limitations, and future experimental directions.

2 Background

2.1 Monitoring Prosthetic Socket Use: Current Methods and Limitations

The measurement of prosthetic wear time has evolved through several methodological stages, each with characteristic strengths and limitations. Self-report diaries, the most widely used approach, require participants to record daily donning and doffing times. While straightforward to implement, this method depends on participant compliance and is vulnerable to systematic biases; retrospective reports tend to overestimate wear duration, and diary fatigue over multi-week recording periods can degrade data quality [1].

Accelerometry-based approaches, using devices such as the ActiGraph GT3X, provide objective step-count data that can serve as an indirect proxy for prosthetic use. The Limbkit study employed ActiGraph step counters across two three-week phases, but encountered practical challenges including limited recording capacity (21 d to 42 d), dependence on legacy software (ActiLife version 6.5.3) installed on only three dedicated computers, and undetected device malfunctions that were discovered only upon device retrieval from participants. Commercial fitness trackers offer a lower-cost alternative for step counting but share the same core limitation. However, step counts cannot distinguish between prosthetic use and non-prosthetic ambulation (e.g., wheelchair use with leg movement), nor do they capture static standing or seated wearing time. Pressure-sensitive insole systems such as SurroSense Rx/Orpyx detect weight-bearing but require integration into the shoe rather than the socket, and do not measure non-weight-bearing wear time [28].

Temperature-based monitoring represents the most direct approach to prosthetic use measurement. The fundamental principle is straightforward: when a device is worn against the body, the internal temperature rises above ambient levels due to metabolic heat transfer. The Orthotimer system implements this principle through a miniature thermistor that samples temperature at 15 min intervals, classifying each measurement as "worn" or "not worn" based on a threshold algorithm [3]. The validation study by Lutjeboer et al. demonstrated that the choice of classification algorithm substantially affects accuracy: the "Groningen algorithm," which accounts for gradual temperature transitions, achieved $r = 0.995$ correlation with camera-verified ground truth, whereas the manufacturer's default algorithm-29 (using the 29 °C threshold) achieved only $r = 0.680$ [3].

The Orthotimer has been successfully deployed for shoulder abduction brace compliance monitoring after rotator cuff repair [26], diabetic footwear adherence assessment [5], foot

orthosis wear time measurement [6], and pelvic orthosis trials [27]. In all these applications, the sensor is positioned in close thermal proximity to the skin with minimal intervening material (<1 mm of padding or tape, as recommended by the manufacturer). The prosthetic socket environment fundamentally violates this proximity requirement, as we quantify in Section 3.

2.2 Graphene Nanoribbon Sensors: Relevant Properties

Graphene nanoribbons exhibit a width-dependent band gap $E_g = 2\pi\hbar v_F/(3W) \approx 1.38/W$ eV·nm, where W is the ribbon width in nanometres [19–21]. This tuneable band gap, combined with graphene's exceptional thermal conductivity ($\kappa \approx 5000\,\mathrm{W\,m^{-1}\,K^{-1}}$), high carrier mobility ($\mu \approx 200\,000\,\mathrm{cm^2\,V^{-1}\,s^{-1}}$), and mechanical flexibility (Young's modulus $\sim$1 TPa), makes GNRs ideal candidates for multi-functional sensing elements in conformal, mechanically demanding environments such as prosthetic sockets [11, 14].

For temperature sensing specifically, two quantum mechanical mechanisms are relevant, and because they may be unfamiliar to readers outside condensed matter physics we develop both in some detail here, with Figure 2 providing a graphical guide.

The first mechanism is the quantum capacitance of graphene, an electrical readout of the density of electronic states. Unlike an ordinary capacitor, whose capacitance is fixed by geometry, a graphene channel presents an additional capacitance in series that depends on how many electronic states are available at the Fermi level, and this availability changes with temperature. At low temperatures the quantum capacitance scales linearly with $|E_F|$, and at elevated temperatures it acquires a T^2 correction [22], so that a measurement of capacitance becomes a measurement of temperature (Fig. 2c). The temperature coefficient $\pi^2 k_B^2 T/(3E_F^2)$ arising from this correction is the intrinsic thermal response that the Lambert W mechanism amplifies in Section 4.

The second mechanism is shot noise thermometry, which deserves a fuller explanation because it provides something rare in thermometry: an absolute temperature measurement requiring no calibration. Electrical current is carried by discrete charges, and the resulting statistical fluctuations (shot noise) compete with thermal agitation of the carriers (Johnson noise). The current noise spectral density of a biased conductor interpolates between the two regimes:

$$S_I = 2eI \coth\left(\frac{eV}{2k_B T}\right), \tag{1}$$

where e is the electron charge, I the current, V the bias voltage, and T the carrier temperature. At low bias ($eV \ll 2k_B T$) thermal noise dominates and $S_I \to 4k_B T G$; at high bias ($eV \gg 2k_B T$) pure shot noise dominates and $S_I \to 2eI$. The crossover between the two regimes occurs at $eV \approx 2k_B T$ (Fig. 2a), so the bias voltage at which the measured noise changes character directly reveals the temperature through fundamental constants alone, with no reference thermometer required [15, 23]. For the present application, the relevant signal is the change in the noise characteristic produced by the small liner-attenuated temperature shift at the sensor; as Fig. 2b shows, a 3 K sensor-side shift produces a fractional noise change at low bias that is well within modern readout precision. Graphene's low Johnson noise and high mobility make it an excellent platform for this technique, with demonstrated precision below 10 mK at cryogenic temperatures [15].

Recent experimental work has established the feasibility of graphene-based wearable thermal sensing. Kang et al. developed a wireless graphene thermal patch providing continuous temperature mapping over a $3\,\mathrm{cm} \times 3\,\mathrm{cm}$ skin area with sub-$0.1\,^{\circ}\mathrm{C}$ resolution, incorporating both sensing and thermotherapy functions [24]. Graphene-polymer composites have been integrated into flexible textile substrates, demonstrating durable sensing with conductivities of $592\,\mathrm{S\,m^{-1}}$ and stability over 2000 strain cycles [25]. These advances indicate that graphene-based sensors are already approaching the performance envelope required for integration into the prosthetic socket environment.

3 Quantitative Analysis of the Thermal Barrier Problem

To understand why a fixed-threshold thermistor fails in prosthetic sockets, we develop a one-dimensional steady-state heat transfer model for the residual limb–liner–socket–sensor system, summarised graphically in Figure 3. The residual limb surface temperature T_{skin} is maintained at approximately $33\,^{\circ}\mathrm{C}$ to $36\,^{\circ}\mathrm{C}$ by metabolic heat generation, with the lower end of this range corresponding to sedentary periods or cool environments [8]. The temperature at the sensor position T_{sensor} depends on the ambient temperature T_{amb} and on how the total thermal resistance is partitioned between the sensor's interior (skin-facing) side and its exterior (ambient-facing) side.

Let R_{int} denote the thermal resistance per unit area between the skin and the sensor and R_{ext} that between the sensor and the ambient, with $R_{\mathrm{total}} = R_{\mathrm{int}} + R_{\mathrm{ext}}$. The steady-state heat flux is uniform through all layers, and the temperature drop across each layer is proportional to its resistance, giving:

$$T_{\mathrm{sensor}} = T_{\mathrm{amb}} + \frac{R_{\mathrm{ext}}}{R_{\mathrm{total}}}(T_{\mathrm{skin}} - T_{\mathrm{amb}}). \tag{2}$$

For a sensor embedded between the liner and the socket wall (the geometry relevant to a wall-mounted Orthotimer), $R_{\mathrm{int}} = R_{\mathrm{liner}}$ and $R_{\mathrm{ext}} = R_{\mathrm{socket}} + R_{\mathrm{out}}$, where $R_{\mathrm{liner}} = d_{\mathrm{liner}}/k_{\mathrm{silicone}}$, $R_{\mathrm{socket}} = d_{\mathrm{socket}}/k_{\mathrm{PETG}}$, and $R_{\mathrm{out}} = 1/h$ is the external convective resistance.

Using representative parameter values, liner thickness $d_{\mathrm{liner}} = 5\,\mathrm{mm}$, silicone conductivity $k_{\mathrm{silicone}} = 0.2\,\mathrm{W\,m^{-1}\,K^{-1}}$, PETG socket wall thickness $d_{\mathrm{socket}} = 4\,\mathrm{mm}$, PETG conductivity $k_{\mathrm{PETG}} = 0.18\,\mathrm{W\,m^{-1}\,K^{-1}}$, natural convection coefficient $h = 10\,\mathrm{W\,m^{-2}\,K^{-1}}$, $T_{\mathrm{skin}} = 34\,^{\circ}\mathrm{C}$, and $T_{\mathrm{amb}} = 22\,^{\circ}\mathrm{C}$, the individual resistances per unit area are $R_{\mathrm{liner}} = 0.025\,\mathrm{K\,m^2\,W^{-1}}$, $R_{\mathrm{socket}} = 0.022\,\mathrm{K\,m^2\,W^{-1}}$, and $R_{\mathrm{out}} = 0.100\,\mathrm{K\,m^2\,W^{-1}}$, summing to $R_{\mathrm{total}} = 0.147\,\mathrm{K\,m^2\,W^{-1}}$. Substituting into Eq. (2) gives:

$$T_{\mathrm{sensor}} = 22 + \frac{0.022 + 0.100}{0.147}\,(12) \approx 32.0\,^{\circ}\mathrm{C}. \tag{3}$$

This baseline estimate of $32.0\,^{\circ}\mathrm{C}$ sits above the $29\,^{\circ}\mathrm{C}$ threshold, so that detection would in principle succeed under idealised conditions. The Limbkit observations of systematic zero-hour wear time, however, indicate that this margin is regularly eroded in practice. Several mechanisms act in the same direction, and combine to push the sensor-side temperature

below threshold. Imperfect thermal contact between the liner and the inner socket wall introduces interfacial resistance not captured in the idealised model; localised air gaps from socket misfit add an insulating layer with conductivity an order of magnitude lower than silicone; ambient temperatures common in Canadian indoor environments and outdoor seasonal conditions can fall well below 22 °C, shifting the entire profile downward; and reduced metabolic activity during sedentary periods lowers T_{skin} toward the bottom of its physiological range. As a concrete illustration, dropping T_{skin} to 30 °C while holding other parameters fixed gives $T_{\text{sensor}} \approx 28.6\,^{\circ}\text{C}$, below threshold. An additional $0.05\,\text{K}\,\text{m}^2\,\text{W}^{-1}$ of contact and air-gap resistance on the interior side under the original conditions reduces T_{sensor} to 29.4 °C, eroding the margin to within half a degree of the threshold; when this added resistance coincides with the reduced skin temperature, the sensor reads $T_{\text{sensor}} \approx 27.0\,^{\circ}\text{C}$, well below threshold. Detection failure thus emerges not from any single extreme condition but from the conjunction of entirely ordinary ones, as mapped across the parameter space in Figure 3.

Because the dominant thermal barrier is the silicone liner rather than the socket wall, this detection failure applies to any liner-based socket, including conventionally laminated or thermoformed sockets, and is not specific to 3D-printed PETG.

The critical design parameter exposed by this analysis is the minimum detectable temperature differential at the sensor, $\Delta T_{\text{min}} = T_{\text{sensor}} - T_{\text{amb}}$. For the Orthotimer with its fixed 29 °C threshold and $T_{\text{amb}} = 22\,^{\circ}\text{C}$, the algorithmic requirement is $\Delta T_{\text{min}} = 7\,^{\circ}\text{C}$, whereas the differential actually available through the liner–socket barrier under unfavourable but realistic conditions may be only 3 °C to 5 °C. A sensor capable of reliably detecting differentials well below 1 °C would eliminate the thermal barrier problem entirely.

4 Lambert W Enhanced Temperature Sensing Framework

Having established what the thermal barrier costs, we now turn to the mathematical mechanism that recovers it. The central idea, developed in plain terms before the formalism, is that a sensor can be operated at a special "tipping point" of its governing equations where its response to small changes is dramatically amplified, in the same way that a ball balanced near the crest of a hill moves much further for a given nudge than one resting in a valley. For GNR sensors this tipping point is the branch point of the Lambert W function, and the remainder of this section quantifies how close to it a practical sensor can operate and how much amplification results.

4.1 The Lambert W Function and Branch-Point Singularity

The Lambert W function arises as the solution to the transcendental equation $We^W = z$ and plays a fundamental role in the quantum mechanics of confinement, providing exact analytical solutions to the finite square well (FSW) problem [16–18]. The derivative of the Lambert W function,

$$\frac{dW}{dz} = \frac{W(z)}{z[1+W(z)]} = \frac{1}{e^{W(z)}[1+W(z)]}, \tag{4}$$

diverges as $W \to -1$ (equivalently, $z \to -1/e$). Using the Puiseux expansion $W(z) \approx -1 + \sqrt{2(ez+1)}$ near the branch point yields the enhancement factor:

$$\eta_{\text{enh}} \equiv \left| \frac{dW}{dz} \right| \approx \frac{1}{\sqrt{2\delta/e}} \propto \delta^{-1/2}, \tag{5}$$

where $\delta = z - z_c$ is the distance from the branch point $z_c = -1/e$ [15]. This singularity provides a systematic mechanism for sensitivity amplification. At $\delta = 0.1$, the enhancement factor is $\eta_{\text{enh}} = 2.48$; at $\delta = 0.01$, 10.10; at $\delta = 0.001$, 35.14; and at $\delta = 0.0001$, 114.8, values verified numerically in the companion framework paper [15] and reproduced in Figure 4.

4.2 Temperature Sensitivity of Graphene Nanoribbon Sensors

For GNR sensors, the Lambert W operating point z is governed by the ratio of thermal energy to confinement energy:

$$z \propto -\exp\left(-\frac{E_g}{k_B T}\right), \tag{6}$$

where E_g is the band gap and T is the temperature [15]. Ribbons with $E_g \sim k_B T$ operate near the branch point, where enhancement is maximised. At body temperature ($T \approx 310\,\text{K}$, $k_B T \approx 27\,\text{meV}$), this resonance condition corresponds to a ribbon width

$$W_{\text{opt}} \sim \frac{1.38\ \text{eV}\cdot\text{nm}}{k_B T} \approx 51\,\text{nm} \tag{7}$$

for maximum thermal sensitivity. The Lambert W enhanced temperature sensitivity combines quantum capacitance and FSW energy-level shifts [15]:

$$S_T^W = \frac{W_k}{z(1+W_k)} \cdot \frac{\pi^2 k_B^2 T}{3E_F^2}, \tag{8}$$

where the first factor is the Lambert W enhancement and the second the intrinsic thermal response of the electronic system developed in Section 2.2. The critical insight is that the enhancement factor $(1+W_k)^{-1}$ amplifies the thermal signal independently of the magnitude of the temperature differential, allowing detection of the small ΔT values transmitted through prosthetic liner barriers.

4.3 Minimum Detectable Temperature Through a Prosthetic Liner

Combining the thermal barrier analysis of Section 3 with the Lambert W enhancement framework, we estimate the minimum detectable temperature differential for a GNR sensor embedded in a prosthetic socket. For a resistance-based readout, the noise-equivalent temperature difference (NETD) in the Johnson-noise-limited regime is:

$$\text{NETD} = \frac{\sqrt{4k_B T_0 R\,\Delta f}}{\alpha R I \cdot \eta_{\text{enh}}}, \tag{9}$$

where T_0 is the operating temperature, R is the sensor resistance, Δf is the measurement bandwidth, $\alpha = (1/R)(dR/dT)$ is the temperature coefficient of resistance, I is the bias current, and η_{enh} is the Lambert W enhancement factor.

For a GNR sensor with $\alpha \approx -0.01\,\text{K}^{-1}$ (comparable to demonstrated graphene thermistors [24]), $R = 10\,\text{k}\Omega$, $I = 1\,\mu\text{A}$, $\Delta f = 1\,\text{Hz}$ (appropriate for wear-time monitoring with sampling intervals on the order of seconds), $T_0 = 300\,\text{K}$, and $\eta_{\text{enh}} = 35$ at $\delta = 0.001$, the Johnson noise voltage is

$$\sqrt{4k_B T_0 R\,\Delta f} \approx 1.29 \times 10^{-8}\,\text{V}, \tag{10}$$

and the voltage responsivity is $\alpha R I \cdot \eta_{\text{enh}} = 0.01 \times 10^4 \times 10^{-6} \times 35 \approx 3.5 \times 10^{-3}\,\text{V}\,\text{K}^{-1}$, giving $\text{NETD}_{\text{Johnson}} \approx 3.7\,\mu\text{K}$.

This Johnson-noise floor is far below the precision required for wear-time detection; in practice, the achievable NETD is set by $1/f$ noise, contact fluctuations, and environmental drift. Taking the Kang et al. wireless graphene thermal patch [24], which demonstrates roughly 0.1 °C resolution under realistic wearable conditions *without* branch-point enhancement, as a more conservative baseline, the Lambert W mechanism provides an additional η_{enh}-fold reduction in NETD. At $\delta = 0.001$, this yields a practical NETD of approximately 3 mK; even at the more relaxed operating point $\delta = 0.01$ (10-fold enhancement), the projected NETD remains near 10 mK. In either case, the resolution is two to three orders of magnitude finer than the 3 °C to 5 °C differential available through the liner barrier, providing comfortable signal-to-noise margin even accounting for practical degradation factors, as visualised in Figure 5. The framework therefore predicts that a Lambert W enhanced GNR sensor can reliably resolve attenuated thermal signals that fixed-threshold thermistors miss.

4.4 Practical Considerations for Branch-Point Operation

Operating near the branch point requires tuning E_g relative to $k_B T$ with high precision. From Eq. (6), $\delta = 0.001$ corresponds to $|\Delta E_g / k_B T| \approx 0.003$, or $\Delta E_g \approx 0.08\,\text{meV}$ at body temperature. This is achievable by electrostatic gating, electrochemical doping, or controlled mechanical pre-strain of an individual device after fabrication, but is substantially tighter than typical lithographic width tolerances. The companion framework paper quantifies the resulting practical floor as $\delta_{\min} \sim 10^{-4}$–$10^{-3}$ from state-of-the-art width tolerances, with closed-loop gate stabilisation of $E_g/k_B T$ to about 0.3 % required to hold a target $\delta \sim 10^{-3}$ [15]. Practical sensor designs therefore require either post-fabrication tuning, operation at a more relaxed $\delta \sim 0.01$–0.05 where enhancement is still 5–10-fold, or arrays of ribbons with slightly different widths from which the closest-to-resonance device is selected at calibration. These strategies relax the manufacturing challenge while preserving most of the sensitivity gain.

5 Multi-Modal Sensing Architecture

A key advantage of GNR sensors over single-function thermistors is the ability to simultaneously detect multiple physical parameters through distinct transduction mechanisms. This multi-modal capability provides redundant verification of prosthetic wear state, eliminates the single-point-of-failure vulnerability that compromised the Orthotimer deployment in the

Limbkit study, and, looking beyond adherence measurement, opens a path toward continuous monitoring of the pressures, strains, and microclimate conditions implicated in skin breakdown at the limb–socket interface.

5.1 Temperature Channel

As developed in Section 4, the thermal sensing channel exploits the Lambert W enhanced temperature sensitivity of Eq. (8). For prosthetic socket monitoring, the sensor detects the temperature differential between the liner-transmitted body heat and the ambient environment. The classification criterion for "worn" status is $\Delta T > k \cdot \mathrm{NETD}$ for a suitably chosen confidence factor k (typically $k = 3$ for 99.7% reliability), with the NETD reduced by the enhancement factor η_{enh} to enable detection through the liner barrier.

5.2 Pressure Channel

When the prosthetic socket is donned and weight is applied, the residual limb exerts pressure on the socket wall. GNR sensors respond to pressure indirectly: applied stress P produces strain $\varepsilon = P/Y_{\mathrm{wall}}$ in the socket wall (where Y_{wall} is the wall material's Young's modulus), which couples into the GNR through the strain-dependent hopping parameter. The resulting band gap modification follows $E_g(\varepsilon) = E_g^0(1+\beta\varepsilon)$, where $\beta \approx 3.37$ is the Grüneisen parameter for graphene [15]. The fractional sensitivity to pressure is then

$$S_P = \frac{1}{E_g}\frac{dE_g}{dP} = \frac{\beta}{Y_{\mathrm{wall}}}, \tag{11}$$

which, with Lambert W enhancement applied universally across modalities, gives

$$S_P^W = \frac{\beta}{Y_{\mathrm{wall}}} \cdot \frac{W_k}{1+W_k}. \tag{12}$$

For a PETG socket wall ($Y_{\mathrm{wall}} \approx 2\,\mathrm{GPa}$), $S_P \approx 1.7 \times 10^{-9}\,\mathrm{Pa}^{-1}$. The 10 kPa to 100 kPa pressures typical of socket loading during stance and ambulation [8] thus produce fractional band gap changes of $\sim 10^{-5}$–10^{-4} at the bare-sensitivity level. With the 35-fold Lambert W enhancement, these fractional changes rise to $\sim 10^{-3}$, well within the readout precision of modern integrated circuits.

A practical concern for any interface pressure sensor is creep and hysteresis, the drift and history dependence that degrade elastomeric and foam-based pressure-mapping systems in prolonged use [4]. The transduction mechanism here differs in a way that is favourable in principle: the pressure signal is carried by the elastic band-gap response of the covalently bonded graphene lattice (Young's modulus $\sim$1 TPa, with demonstrated stability over thousands of strain cycles [25]) rather than by the compression of a viscoelastic medium. Residual creep will instead enter through the PETG wall and any polymer encapsulation, whose viscoelastic relaxation transfers slowly varying strain to the sensor. Characterising this substrate-limited drift, and confirming that it remains small compared with the donning and doffing signals of interest, is an explicit target of the experimental programme outlined in Section 7. If confirmed, the low-creep behaviour would give the platform applications well beyond prosthetics, across skin–device interfaces where current pressure-mapping technologies fall short.

5.3 Strain Channel

The mechanical deformation of the PETG socket wall under loading also produces measurable strain at the sensor location, which can be detected directly through the shift of quantised energy levels rather than via the pressure-to-strain conversion of the wall material. GNR sensors detect strain with fractional sensitivity $(1/E_g)(dE_g/dW) = -1/W$ that increases for narrower ribbons [15], giving the Lambert W enhanced response

$$S_\varepsilon^W = \beta \cdot \frac{W_k}{1 + W_k}. \tag{13}$$

This channel provides information complementary to both temperature and pressure: it is insensitive to thermal conditions and responds only to mechanical deformation, enabling discrimination between socket donning (which produces strain, pressure, and temperature signals together) and environmental temperature changes (temperature only).

The strain channel also offers a route toward measuring interface friction and shear, which act alongside pressure in the aetiology of skin breakdown. Interface shear stresses of 5 kPa to 50 kPa transmitted into the PETG wall (shear modulus $G = Y_{\text{wall}}/2(1+\nu) \approx 0.74\,\text{GPa}$ for $\nu = 0.35$) produce wall shear strains of 7×10^{-6} to 7×10^{-5}, one to two orders of magnitude above the framework's predicted 10^{-6} strain resolution [15], with a factor of roughly 27 in margin at a representative 20 kPa (Fig. 9a). A spatial array of strain elements could therefore in principle resolve shear from differential in-plane strain; the multi-element readout and calibration this requires are identified as future work in Section 7.

5.4 Moisture Channel for Skin-Health Monitoring

Skin maceration under sustained high humidity is a recognised contributor to skin breakdown at the limb–socket interface, and temperature alone does not capture the microclimate that drives it. The companion framework paper derives a Lambert W enhanced humidity modality for graphene oxide (GO) sensing elements [15]: physisorbed water enables Grotthuss-mechanism proton conduction with exponential conductivity response $\sigma(\text{RH}) = \sigma_0 \exp(\alpha \cdot \text{RH})$, where $\alpha \approx 0.03$–0.08 per %RH, giving the enhanced sensitivity

$$S_{\text{H}_2\text{O}}^W = \frac{W_k}{z(1 + W_k)} \cdot \alpha, \tag{14}$$

with demonstrated GO response times as fast as 30 ms [15]. At $\delta = 0.001$ and the mid-range $\alpha = 0.05$ per %RH, Eq. (14) evaluates to $S_{\text{H}_2\text{O}}^W \approx 1.76$ per %RH (Fig. 6b), so that sub-percent changes in relative humidity at the interface are readily resolved and sustained excursions into the maceration-risk band above roughly 85 %RH (Fig. 6a) can be flagged.

We position this channel deliberately as a skin-health monitor rather than a wear classifier, for a reason rooted in signal dynamics rather than sensitivity. The fusion rule of Eq. (15) must switch on the timescale of donning and doffing, which the temperature, pressure, and strain channels do: pressure and strain respond essentially instantaneously to load, and the sensor-side temperature settles within minutes. Interface humidity instead lags the wear state in both directions, rising toward saturation over tens of minutes as perspiration accumulates after donning and decaying slowly after doffing as moisture retained in the liner

evaporates, and its baseline is confounded by ambient humidity, liner washing state, and individual perspiration. Weighting such a channel in Eq. (15) would therefore blur the very transitions the classifier exists to detect, producing false positives after doffing and false negatives after donning; the fusion vote of Section 5.5 accordingly remains three-channel. The same slow dynamics are precisely what suit the moisture channel to its assigned role, since maceration risk is defined by sustained rather than instantaneous exposure, and a future probabilistic classifier could still admit humidity as a slowly varying prior on wear state without letting it vote on transitions. The moisture channel thus provides the microclimate record, alongside temperature, that clinicians would consult when interpreting skin irritation or breakdown events.

5.5 Fusion Algorithm

A robust wear-time classification algorithm fuses the three sensing channels through a weighted voting scheme:

$$\mathcal{W}(t) = \begin{cases} 1 & \text{if } w_T S_T(t) + w_P S_P(t) + w_\varepsilon S_\varepsilon(t) > \theta, \\ 0 & \text{otherwise,} \end{cases} \tag{15}$$

where S_T, S_P, S_ε are the normalised sensor signals, w_T, w_P, w_ε are channel weights optimised from calibration data, and θ is a decision threshold. This multi-modal approach ensures that wear-time detection is robust against single-channel failure: if the thermal signal is attenuated below threshold by the liner, the pressure and strain channels still provide definitive identification of socket use; if a participant is stationary and exerts minimal pressure on the wall, the thermal channel alone retains discrimination capability.

To illustrate this robustness quantitatively, Figure 7 presents a simulation of a synthetic 24-hour wearing day, with ground truth wear from 07:00 to 22:00 including a cold outdoor walk (17:00–18:30, ambient 5 °C) during which the liner-attenuated thermal signal collapses, and a sedentary seated period (13:00–15:00) during which wall pressure and strain are minimal. The simulation uses the thermal model of Section 3, additive Gaussian sensor noise, and the fusion rule of Eq. (15) with weights $(w_T, w_P, w_\varepsilon) = (0.4, 0.3, 0.3)$ and threshold $\theta = 0.30$. A thermal-only classifier applying the fixed 29 °C threshold achieves 93.8 % accuracy, misclassifying the entire cold interval as non-wear, whereas the three-channel fusion vote classifies every sample correctly. While illustrative rather than empirical, the simulation demonstrates the structural advantage of the architecture: no single environmental condition can silence all three channels simultaneously.

6 Integration with 3D-Printed Prosthetic Sockets

6.1 Fabrication-Integrated Strategies

The Limbkit project employs a Creality Ender-6 3D printer with transparent PETG filament (1.75 mm diameter) to fabricate custom prosthetic sockets. This fabrication workflow offers an opportunity for sensor integration that is not readily available with conventional socket manufacturing techniques such as thermoforming and lamination. Three primary integration

strategies are compatible with the fused deposition modelling (FDM) process used by the Ender-6.

The first approach is *print-pause-embed*, in which the printing process is paused at a target layer height, a pre-fabricated GNR sensor element is placed on the printed surface, and printing resumes to encapsulate the sensor within the socket wall. This method has been demonstrated for embedding resistive strain gauges and thermocouples in FDM parts, with good adhesion and minimal impact on mechanical integrity [29]. The principal constraint is that sensor leads must be routed out of the print without interfering with subsequent layers.

The second approach involves *surface-applied thin films*, in which a GNR sensor array is deposited on a flexible polymer substrate and bonded to the inner surface of the completed socket using biocompatible adhesive. This post-printing strategy avoids interference with the print process and allows sensor positioning to be optimised independently of socket geometry, at the cost of an additional manufacturing step.

The third approach exploits *graphene-loaded PETG composites*, in which conductive graphene fillers are incorporated into the PETG filament itself, producing a socket wall with intrinsic sensing capability. While this approach is the most ambitious of the three, recent developments in graphene/polymer composite filaments for FDM printing suggest its feasibility [25], and the resulting distributed-sensing geometry would naturally support arrays of measurement locations across the socket interior.

For all three approaches, wireless readout can be achieved using near-field communication (NFC) or Bluetooth Low Energy (BLE) modules, eliminating the wired USB reader required by the Orthotimer system and enabling real-time data transmission to mobile devices or cloud platforms.

6.2 Sensor Placement: Instrumenting the Socket Wall versus the Liner

The three strategies above all place the sensor in or on the socket wall, on the far side of the liner from the residual limb, and the thermal barrier analysis of Section 3 is the price of that choice. The alternative is to instrument the liner itself: a thin flexible sensing film at the residual limb–liner interface, of the kind demonstrated on textile and polymer substrates [24, 25], sits on the warm side of the dominant thermal resistance and is thereby freed from the barrier entirely. Figure 8 quantifies the comparison with the same steady-state model, taking a 0.1 mm film with silicone-like conductivity ($R_{\mathrm{int}} \approx 5 \times 10^{-4}\,\mathrm{K\,m^2\,W^{-1}}$). At baseline conditions the liner-side sensor reads 34.0 °C against 32.0 °C for the wall-embedded sensor; in the cold ambient of the Figure 7 scenario ($T_{\mathrm{amb}} = 5\,^{\circ}\mathrm{C}$) the wall sensor falls to a marginal 29.1 °C while the liner-side sensor holds 33.9 °C, essentially immune to ambient conditions. Contact and air-gap degradation at the liner–socket interface, which pushes the wall-embedded sensor below threshold (Fig. 3c), lies on the liner-side sensor's exterior side and slightly raises its reading (Fig. 8c). Liner instrumentation would additionally place the moisture channel of Section 5.4 directly in the skin microclimate it is meant to monitor.

These thermal advantages come with practical costs that the socket-wall strategies avoid. Liners are consumable components replaced on a different schedule from sockets, are rolled and flexed at every donning and doffing, are washed regularly, and complicate wireless pow-

ering, so a liner-integrated sensor must survive conditions harsher than the protected interior of a printed wall. The Lambert W enhancement is precisely what makes the robust, fabrication-integrated wall placement viable despite its thermal disadvantage; liner instrumentation removes the disadvantage at the cost of these durability constraints. The two placements are complementary rather than competing, and a liner-side thermal and moisture film paired with wall-embedded pressure and strain elements is a natural configuration for the sensorised socket prototype proposed in Section 7.

7 Discussion

7.1 Clinical Implications

The framework presented here addresses a concrete unmet need in prosthetic rehabilitation research: objective, reliable measurement of socket use in liner-based prostheses, demonstrated in the specific context of the 3D-printed sockets of the Limbkit study. The failure of the Orthotimer in the Limbkit study is not an isolated technical malfunction but a fundamental mismatch between sensor design assumptions (thin padding, near-skin placement) and the prosthetic socket environment (thick liner, multi-layer thermal barrier). This mismatch will persist for any conventional thermistor-based approach operating with fixed temperature thresholds, regardless of the specific manufacturer or device, and, as shown in Section 3, for any liner-based socket regardless of fabrication method.

The Lambert W enhanced GNR sensor framework resolves this mismatch by reducing the minimum detectable temperature differential by two to three orders of magnitude, and the placement analysis of Section 6.2 shows that instrumenting the liner removes the thermal barrier at its source. The $\delta^{-1/2}$ enhancement scaling provides a systematic design parameter that can be tuned to match specific liner thicknesses and socket geometries, offering predictable performance across diverse clinical scenarios. The multi-modal architecture further ensures robustness by providing pressure and strain channels that are unaffected by the thermal barrier, and these same channels, together with the moisture channel of Section 5.4, offer a longer-term route toward monitoring interface loading and microclimate relevant to skin health, including the possibility of identifying conditions conducive to skin breakdown before damage occurs.

Reliable wear-time data are essential for interpreting step-count and functional outcomes across the full spectrum of prosthetic rehabilitation research, including randomised controlled trials, cohort and other observational studies, and single-subject experimental designs such as the Limbkit study's A-B phase structure. In any of these designs, changes in step counts or performance measures may reflect variation in adherence rather than genuine differences in prosthetic performance if wear time is not separately and objectively quantified. The proposed sensing framework would provide this critical contextual data continuously and objectively, supporting unambiguous attribution of outcome changes to specific intervention components and strengthening causal inference irrespective of the underlying study design.

The GNR sensor approach is distinctive among the alternatives reviewed in Section 2.1 in combining direct wear-time measurement with multi-modal sensing in a single compact element that can be integrated into the socket during fabrication. The Lambert W en-

hancement mechanism provides a theoretical performance ceiling that substantially exceeds conventional sensor technologies, and the analytical framework enables a priori performance prediction for any given socket–liner configuration.

7.2 Interpreting Wear-Time Data in Clinical Context

Wear-time data require careful interpretation, and more wear is not inherently better. Ideally a person should be able to wear the prosthesis whenever they ambulate; a recording of zero wear most likely signals a problem with the fit or function of the device rather than a motivational one. Between those poles, wearing patterns carry meaning that raw hours do not: some users doff the prosthesis between bouts of ambulation, which may be entirely appropriate unless donning and doffing are themselves burdensome, and clinicians may deliberately prescribe graduated wear schedules to build wearing tolerance during early rehabilitation, in which case rising rather than maximal wear time is the desired trajectory. Objective wear-time data should therefore be paired with self-report and other qualitative methods to determine the appropriateness of an observed pattern, since, as noted in Section 1, only the wearer can supply the reasons behind it.

The multi-modal architecture is well suited to this interpretive pairing. Where a wearing pattern raises questions, the pressure, strain, temperature, and moisture records from the same sensing platform can help explain it: localised pressure or shear concentrations may account for discomfort-driven doffing, and sustained thermal or humidity excursions may flag developing skin problems before breakdown occurs. In this way the platform supports not only the measurement of wearing behaviour but the clinical conversation about it.

7.3 User Experience, Comfort, and Acceptability

A sensor intended to protect skin health must not itself endanger it, and any element interposed at the residual limb–liner interface risks creating a pressure point. A first-order elastic estimate bounds this risk: a sensor inclusion of thickness h locally compresses a liner of thickness d_{liner} by h/d_{liner}, raising local pressure by approximately $\Delta P \approx E_{\text{liner}} h/d_{\text{liner}}$ for effective liner modulus $E_{\text{liner}} \approx 0.5\,\text{MPa}$ (Fig. 9b). A 10 µm graphene film produces $\Delta P \approx 1\,\text{kPa}$, below the 4.3 kPa (32 mmHg) capillary occlusion pressure; a 0.1 mm film produces approximately 10 kPa, comparable to normal socket loading; and the 4.5 mm Orthotimer housing would locally compress a 5 mm liner by 90 %, far beyond the linear-elastic regime, underscoring why rigid commercial housings are unsuited to interface placement. The wall-embedded and composite integration strategies of Section 6 produce no protrusion into the interface at all, and thin-film liner instrumentation keeps the added pressure at or below the capillary threshold.

Other user-facing considerations favour the proposed platform. The added mass of thin-film graphene elements is negligible against the mass of the socket and liner. NFC readout can operate passively, harvesting power from the reading device, while BLE operation requires a small battery whose charging burden must be weighed in design; encapsulation appropriate to the warm, moist environment (Section 7.4) simultaneously addresses routine cleaning of the liner and socket. Whether users and prosthetists find a sensorised socket acceptable in daily practice, including perceptions of monitoring, data sharing, and added maintenance,

is an empirical question that the framework cannot answer; acceptability evaluation with prosthesis users and prosthetists is therefore included in the experimental programme below.

7.4 Limitations and Future Work

This paper presents a theoretical framework; therefore, experimental validation is required to confirm the predicted performance in realistic prosthetic socket conditions. Several specific challenges must be addressed in future work. First, GNR fabrication with controlled ribbon widths in the 10 nm to 50 nm range required for thermal-resonance operation relies on electron-beam lithography, chemical synthesis, or atomically precise bottom-up methods that are not yet compatible with clinical-scale production; arrays of slightly mistuned ribbons with post-fabrication selection (Section 4.4) offer a pragmatic interim path. Second, the long-term stability of graphene sensors in the warm, moist socket environment requires investigation, as humidity and perspiration may shift the operating point and degrade the sensor through oxidation or contamination. Third, the biocompatibility of graphene-based materials in prolonged skin-proximate contact, while supported by current evidence for encapsulated devices, must be established for the specific composite formulations envisaged here through appropriate ISO 10993-class testing protocols. Fourth, the creep and hysteresis behaviour of the encapsulated sensor stack under sustained loading, discussed in Section 5, must be characterised before the pressure channel can be used quantitatively for interface health monitoring rather than binary wear classification. Fifth, the placement, shear, and pressure-point analyses of Sections 5.3, 6.2, and 7.3 rest on first-order assumptions, a 0.1 mm film with silicone-like conductivity, linear-elastic inclusion mechanics, and uniform shear transmission into the wall, each of which requires experimental characterisation, and the durability of liner-integrated elements under repeated donning, flexing, and washing is untested.

Nearer-term experimental steps include characterising the thermal attenuation profile through representative liner–socket assemblies using thermocouple arrays, in both wall-embedded and liner-side configurations; benchmarking commercially available graphene thermistor elements against the Orthotimer in a controlled socket mock-up; developing the multimodal fusion algorithm using simultaneous temperature, pressure, and strain measurements from a sensorised socket prototype, for which the simulation of Figure 7 provides the algorithmic template; and evaluating comfort and acceptability of the sensorised socket and liner with prosthesis users and prosthetists. These steps would provide the empirical foundation for translating the Lambert W theoretical predictions into a clinically deployable technology.

8 Conclusion

The objective measurement of prosthetic socket use is a critical methodological need in rehabilitation research that existing sensor technologies do not adequately address. The Orthotimer thermal sensor, while validated for orthotic applications, fails systematically in prosthetic sockets due to the thermal insulation provided by silicone liners under realistic ambient and metabolic conditions, a failure mode common to all liner-based sockets. We have presented a theoretical framework based on graphene nanoribbon quantum sensors that

overcomes this limitation through the Lambert W function sensitivity enhancement mechanism, established and verified in a recently published companion paper, projecting practical noise-equivalent temperature differences in the few-millikelvin range, well within the resolution needed to detect body heat through prosthetic liner barriers, and showing further that instrumenting the liner itself removes the thermal barrier at its source. The proposed multimodal sensing architecture, combining temperature, pressure, and strain channels through a unified Lambert W framework, provides robust and redundant wear-time classification that eliminates the single-point-of-failure vulnerability of temperature-only approaches, as demonstrated in simulation, while the added moisture channel and the shear-resolving potential of the strain channel offer a longer-term route toward monitoring the interface loading and microclimate implicated in skin breakdown. Positioned as a complement to self-report rather than a replacement for it, and designed with sensor form factors that avoid creating the very pressure points the platform is meant to detect, this approach integrates with 3D-printed PETG socket fabrication workflows to offer a practical pathway to clinical deployment. This work establishes the theoretical foundation for a new class of smart prosthetic sockets with embedded quantum-enhanced sensing, with the potential to transform adherence monitoring and interface health assessment in rehabilitation research and clinical practice.

Ethics declarations

The Limbkit study was approved by the University of British Columbia Behavioural Research Ethics Board (certificate H22-03708). All participants provided written informed consent. All methods were carried out in accordance with relevant guidelines and regulations.

Data availability

All quantitative results in this paper are reproduced by an open verification notebook (Google Colab, Python) that regenerates Figures 1–9 and verifies twenty-two numerical claims, comprising the enhancement factors, all thermal scenarios for both sensor placements, the complete noise-equivalent temperature difference chain, the optimal ribbon width, the pressure and humidity sensitivities, the shear-strain detectability estimate, and the sensor form-factor pressure analysis, against independent recomputation from first principles using scipy.special.lambertw; all twenty-two checks pass. The notebook is available from the corresponding author on reasonable request.

Acknowledgements

The authors acknowledge the Limbkit research team and the Centre for Aging SMART for providing access to the step counter and Orthotimer technologies. F.A.C. acknowledges support from the Peaceful Society, Science and Innovation Foundation.

Funding

This research was supported by funding from the Amputee Coalition of Canada (F22-05611) and War Amps (F24-00369).

Author contributions

F.A.C. conceived the theoretical framework, performed the analysis, generated the figures, and drafted the manuscript. M.A. led the Limbkit study, contributed the study description, ethics, and funding information, and revised the manuscript. A.A. contributed to the Limbkit study and edited the manuscript. W.C.M. and W.B.M. supervised the Limbkit study, contributed to the clinical framing and scope of the manuscript, and revised the manuscript. All authors reviewed and approved the final manuscript.

Competing interests

The authors declare no competing interests.

References

[1] Dillingham, T. R., Pezzin, L. E. & MacKenzie, E. J. Limb amputation and limb deficiency: epidemiology and recent trends in the United States. *South. Med. J.* **95**, 875–883 (2005).

[2] Gailey, R. *et al.* Unilateral lower-limb loss: prosthetic device use and functional outcomes in servicemembers from Vietnam War and OIF/OEF conflicts. *J. Rehabil. Res. Dev.* **45**, 15–29 (2008).

[3] Lutjeboer, T., van Netten, J. J., Postema, K. & Hijmans, J. M. Validity and feasibility of a temperature sensor for measuring use and non-use of orthopaedic footwear. *J. Rehabil. Med.* **50**, 920–926 (2018).

[4] Martínez-Cesteros, J., Medrano-Sánchez, C., Castellanos-Ramos, J., Sánchez-Durán, J. A. & Plaza-García, I. Creep and hysteresis compensation in pressure-sensitive mats for improving center-of-pressure measurements. *IEEE Sens. J.* **23**, 29585–29593 (2023). https://doi.org/10.1109/JSEN.2023.3324363

[5] Exterkate, S. H. *et al.* Objectively assessed long-term wearing patterns and predictors of wearing orthopaedic footwear in people with diabetes at moderate-to-high risk of foot ulceration. *J. Foot Ankle Res.* **16**, 60 (2023).

[6] Menz, H. B. & Bonanno, D. R. Objective measurement of foot orthosis wear time using a temperature sensor. *J. Foot Ankle Res.* **14**, 33 (2021).

[7] Klute, G. K., Rowe, G. I., Mamishev, A. V. & Ledoux, W. R. The thermal conductivity of prosthetic sockets and liners. *Prosthet. Orthot. Int.* **31**, 292–299 (2007).

[8] Sanders, J. E. *et al.* Testing of elastomeric liners used in limb prosthetics: classification of 15 products by mechanical performance. *J. Rehabil. Res. Dev.* **41**, 175–186 (2004).

[9] Alkhudair, M., Erenstone, J., Hines, D., Chabot, T., Simpson, E. & Miller, W. C. Limbkit: a portable 3D printing kit for prosthetic sockets. Poster presented at the ISPO 20th World Congress, Stockholm, Sweden (2025).

[10] Alkhudair, M. *Exploring perspectives about 3D printing among rehabilitation professionals and examining the implementation of 3D printed prosthetic sockets for people with lower limb amputation*. Doctoral dissertation, University of British Columbia (2026). (Embargoed; expected release 2028.)

[11] Novoselov, K. S. *et al.* Electric field effect in atomically thin carbon films. *Science* **306**, 666–669 (2004).

[12] Geim, A. K. & Novoselov, K. S. The rise of graphene. *Nat. Mater.* **6**, 183–191 (2007).

[13] Castro Neto, A. H., Guinea, F., Peres, N. M. R., Novoselov, K. S. & Geim, A. K. The electronic properties of graphene. *Rev. Mod. Phys.* **81**, 109–162 (2009).

[14] Katsnelson, M. I. *Graphene: Carbon in Two Dimensions* (Cambridge Univ. Press, 2012).

[15] Chishtie, F. A., Roberts, K., Jisrawi, N., Valluri, S. R., Soni, A. & Deshmukh, P. C. Lambert W function framework for graphene nanoribbon quantum sensing: theory, verification, and multi-modal applications. *Results Eng.* **32**, 112238 (2026). `https://doi.org/10.1016/j.rineng.2026.112238`

[16] Roberts, K. & Valluri, S. R. Tutorial: the Lambert W function in quantum mechanics. *Can. J. Phys.* **95**, 105–110 (2017).

[17] Corless, R. M., Gonnet, G. H., Hare, D. E. G., Jeffrey, D. J. & Knuth, D. E. On the Lambert W function. *Adv. Comput. Math.* **5**, 329–359 (1996).

[18] Valluri, S. R., Gil, M., Jeffrey, D. J. & Basu, S. The Lambert W function and quantum statistics. *J. Math. Phys.* **50**, 102103 (2009).

[19] Son, Y.-W., Cohen, M. L. & Louie, S. G. Energy gaps in graphene nanoribbons. *Phys. Rev. Lett.* **97**, 216803 (2006).

[20] Barone, V., Hod, O. & Scuseria, G. E. Electronic structure and stability of semiconducting graphene nanoribbons. *Nano Lett.* **6**, 2748–2754 (2006).

[21] Chen, Z., Lin, Y.-M., Rooks, M. J. & Avouris, P. Graphene nano-ribbon electronics. *Physica E* **40**, 228–232 (2007).

[22] Xia, J., Chen, F., Li, J. & Tao, N. Measurement of the quantum capacitance of graphene. *Nat. Nanotechnol.* **4**, 505–509 (2009).

[23] Spietz, L., Lehnert, K. W., Siddiqi, I. & Schoelkopf, R. J. Primary electronic thermometry using the shot noise of a tunnel junction. *Science* **300**, 1929–1932 (2003).

[24] Kang, M. *et al.* Wireless graphene-based thermal patch for obtaining temperature distribution and performing thermography. *Sci. Adv.* **8**, eabm6693 (2022).

[25] Zhang, Z. *et al.* Breathable and wearable graphene/waterborne polyurethane coated regenerated PET fabrics for motion sensing and thermal therapy. *Discover Nano* **19**, 61 (2024).

[26] Grubhofer, F., Gerber, C., Meyer, D. C., Wieser, K., Ernstbrunner, L., Catanzaro, S. & Bouaicha, S. Compliance with wearing an abduction brace after arthroscopic rotator cuff repair: a prospective, sensor-controlled study. *Prosthet. Orthot. Int.* **43**, 440–446 (2019). https://doi.org/10.1177/0309364619837794

[27] Halliday, B. *et al.* Evaluating the management of chronic pelvic girdle pain following pregnancy (EMaPP): a randomised controlled feasibility trial. *Pilot Feasibility Stud.* **11**, 54 (2025).

[28] Srass, H., Ead, J. K. & Armstrong, D. G. Adherence and the diabetic foot: high tech meets high touch? *Sensors* **23**, 6898 (2023).

[29] Shemelya, C. *et al.* Anisotropy of thermal conductivity in 3D printed polymer matrix composites for space based cube satellites. *Addit. Manuf.* **16**, 186–196 (2017).

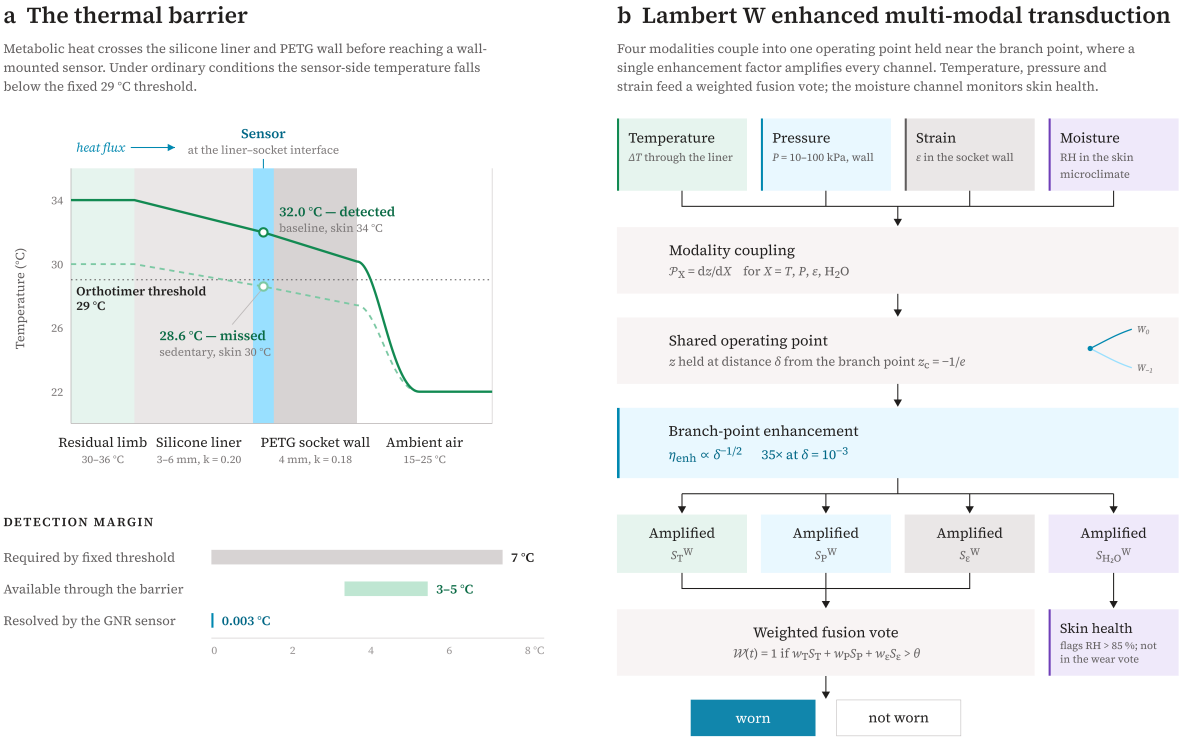


Figure 1: Conceptual map of the sensing framework. (a) The thermal barrier problem: metabolic heat must traverse the silicone liner and PETG socket wall before reaching a wall-mounted sensor, and the resulting temperature profile (red) can fall below the fixed 29 °C detection threshold under realistic conditions. (b) The Lambert W enhanced multi-modal transduction chain: temperature, pressure, strain, and moisture perturbations couple through modality-specific terms $\mathcal{P}_X = dz/dX$ into operating points held near the branch point $z_c = -1/e$, where the same enhancement mechanism $\eta_{\text{enh}} \propto \delta^{-1/2}$ amplifies every channel. Temperature, pressure, and strain feed a weighted fusion vote that classifies the socket as worn or not worn; the moisture channel serves skin-health monitoring rather than wear classification (Section 5.4), since its slow dynamics suit sustained-exposure monitoring but would blur donning and doffing transitions.

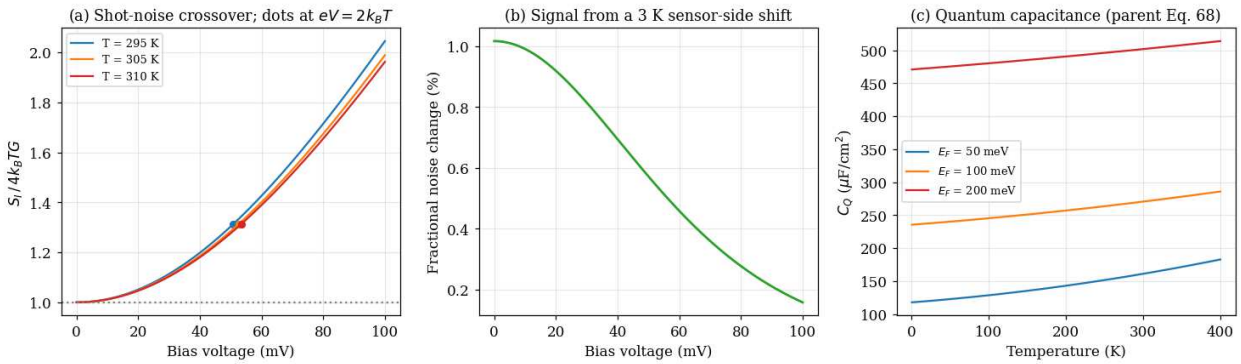


Figure 2: The two quantum thermometric mechanisms available to a GNR sensor. (a) Shot-noise crossover: the normalised current noise spectral density $S_I/4k_BTG$ of Eq. (1) versus bias voltage at three physiologically relevant temperatures; dots mark the calibration-free thermometric point $eV = 2k_BT$. (b) The fractional change in the noise characteristic produced by a 3 K sensor-side temperature shift, the magnitude transmitted through a prosthetic liner, showing that the signal is largest at low bias. (c) Quantum capacitance versus temperature for three Fermi levels, showing the low-temperature plateau and the T^2 growth that provides the intrinsic thermal response amplified by the Lambert W mechanism.

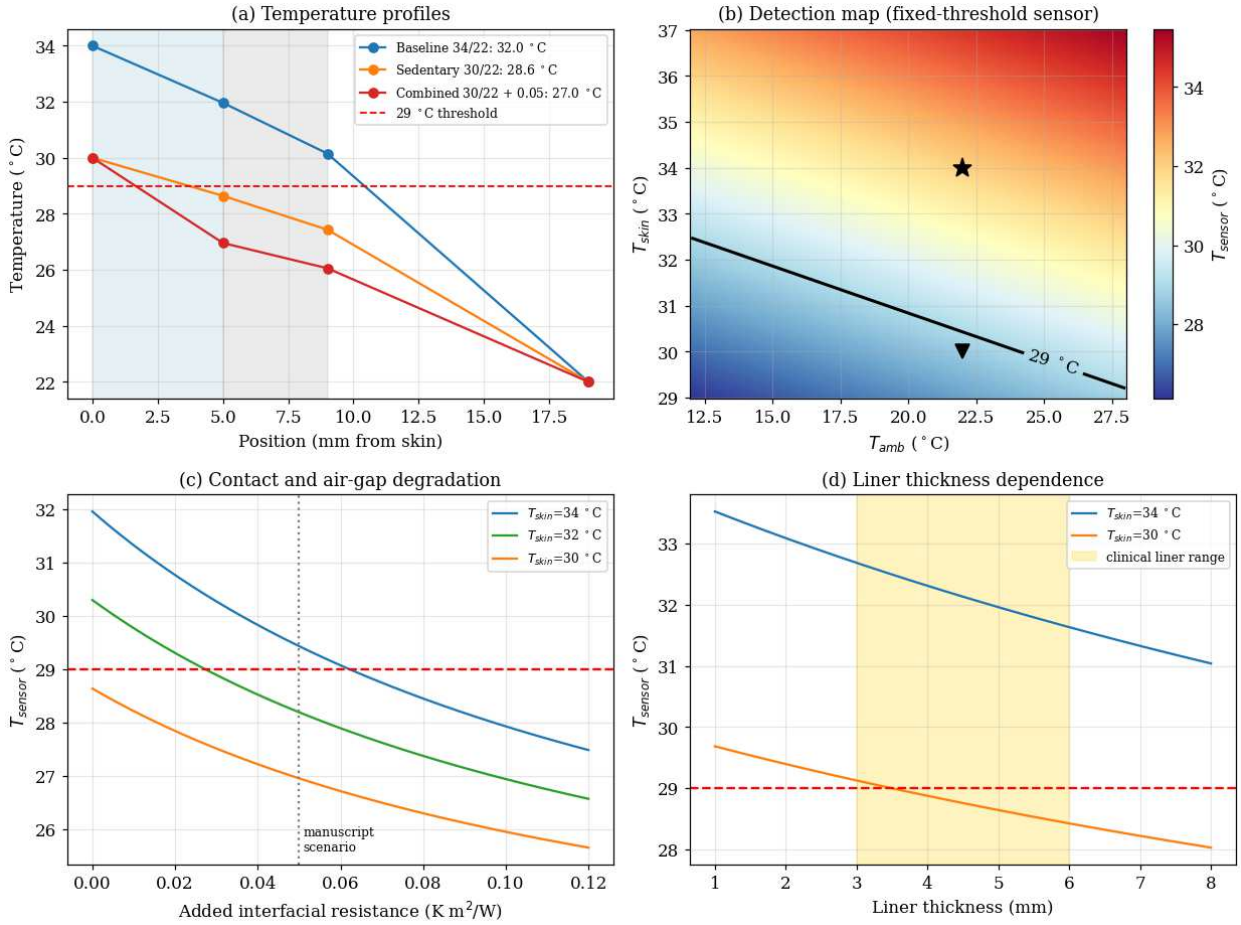


Figure 3: Thermal barrier analysis of the residual limb–liner–socket–sensor system. (a) Steady-state temperature profiles through the layer stack for the baseline (34/22 °C), sedentary (30/22 °C), and combined degraded scenarios; the sensor position is at the liner–socket interface. (b) Sensor temperature over the (T_{amb}, T_{skin}) plane with the 29 °C detection contour; the star marks baseline conditions and the triangle the sedentary scenario. (c) Sensor temperature versus added interfacial contact and air-gap resistance for three skin temperatures. (d) Sensor temperature versus liner thickness across the clinical range of 3 mm to 6 mm. All panels are generated by the open verification notebook.

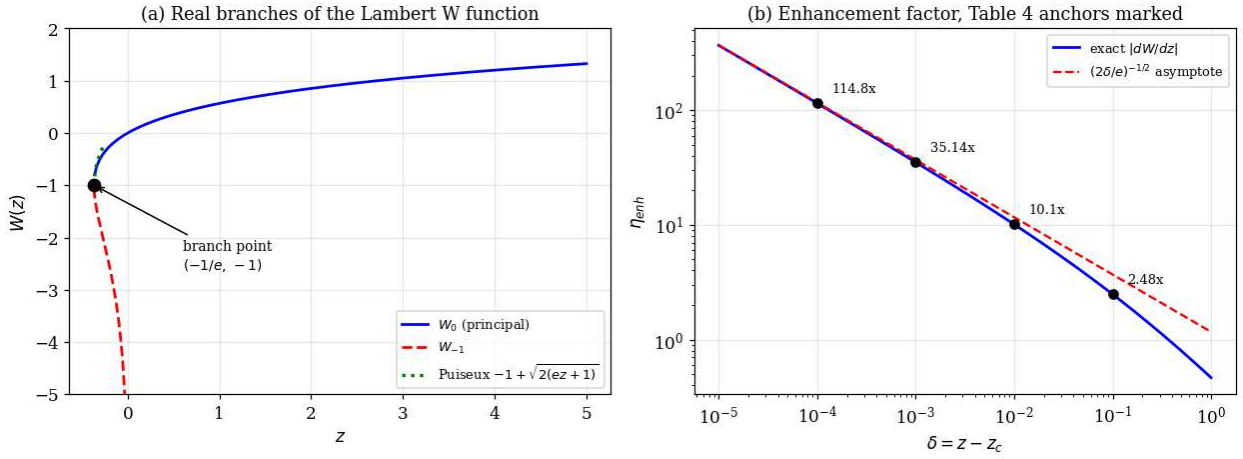


Figure 4: The Lambert W function and its branch-point enhancement. (a) The two real branches W_0 and W_{-1} coalescing at the branch point $(-1/e, -1)$, together with the Puiseux approximation $W \approx -1 + \sqrt{2(ez+1)}$ valid near the branch point. (b) The enhancement factor $\eta_{\text{enh}} = |dW/dz|$ versus the distance δ from the branch point, exhibiting the $\delta^{-1/2}$ scaling of Eq. (5); markers indicate the four operating points tabulated in the companion framework paper [15].

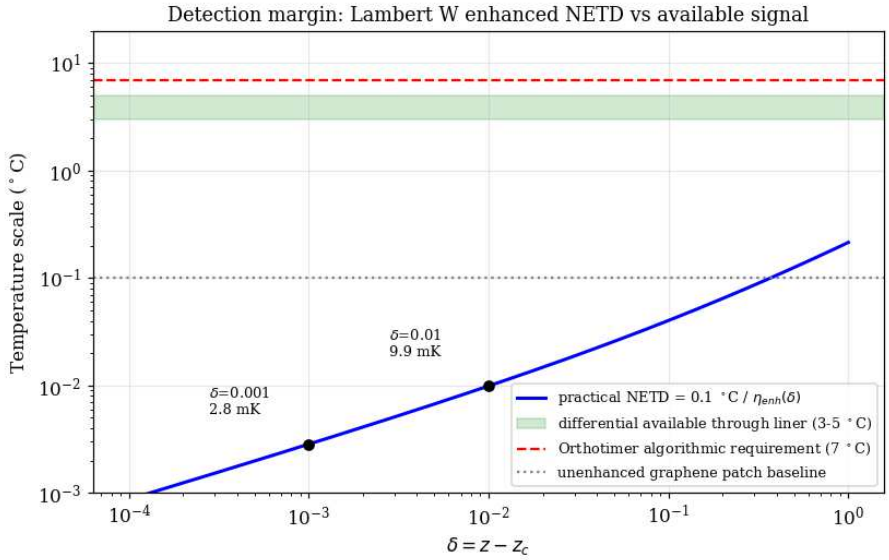


Figure 5: Detection margin of the Lambert W enhanced sensor. The practical noise-equivalent temperature difference (blue), taken as the conservative 0.1 °C wearable graphene baseline [24] divided by the enhancement factor $\eta_{\text{enh}}(\delta)$, is plotted against the operating-point distance δ. The green band marks the 3 °C to 5 °C differential actually available through the liner barrier, and the red dashed line the effective 7 °C requirement of the Orthotimer's fixed-threshold algorithm. At $\delta = 10^{-3}$ the projected NETD of ≈3 mK lies three orders of magnitude below the available signal.

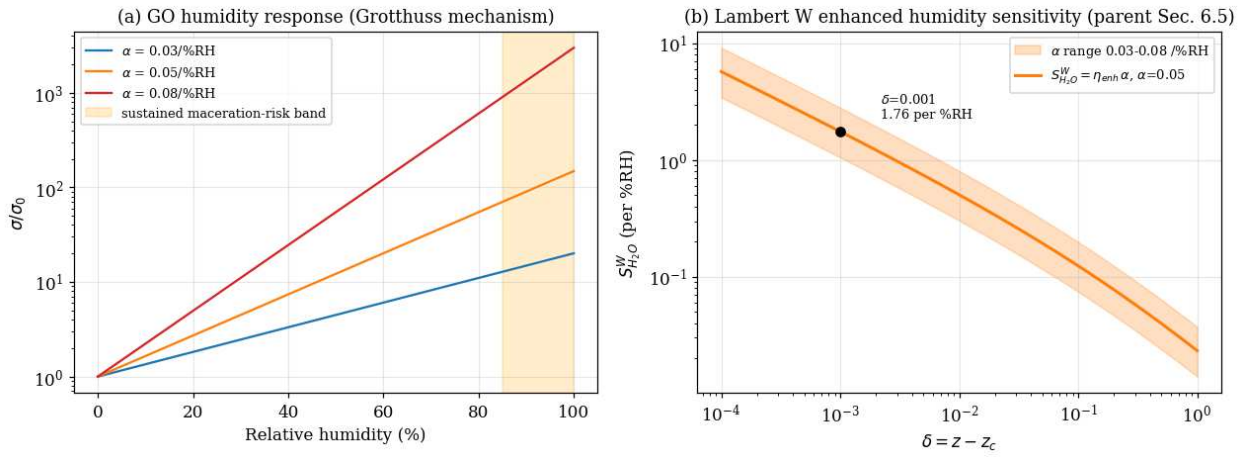


Figure 6: Lambert W enhanced moisture channel for skin-health monitoring. (a) Graphene oxide humidity response $\sigma/\sigma_0 = \exp(\alpha \cdot \mathrm{RH})$ across the reported range $\alpha = 0.03$–0.08 per %RH [15]; the shaded band marks sustained relative humidity above 85 % associated with skin maceration risk. (b) The Lambert W enhanced sensitivity $S^W_{\mathrm{H_2O}} = \eta_{\mathrm{enh}}\,\alpha$ of Eq. (14) versus operating-point distance δ, with the α range shaded; at $\delta = 10^{-3}$ and $\alpha = 0.05$ the sensitivity is 1.76 per %RH.

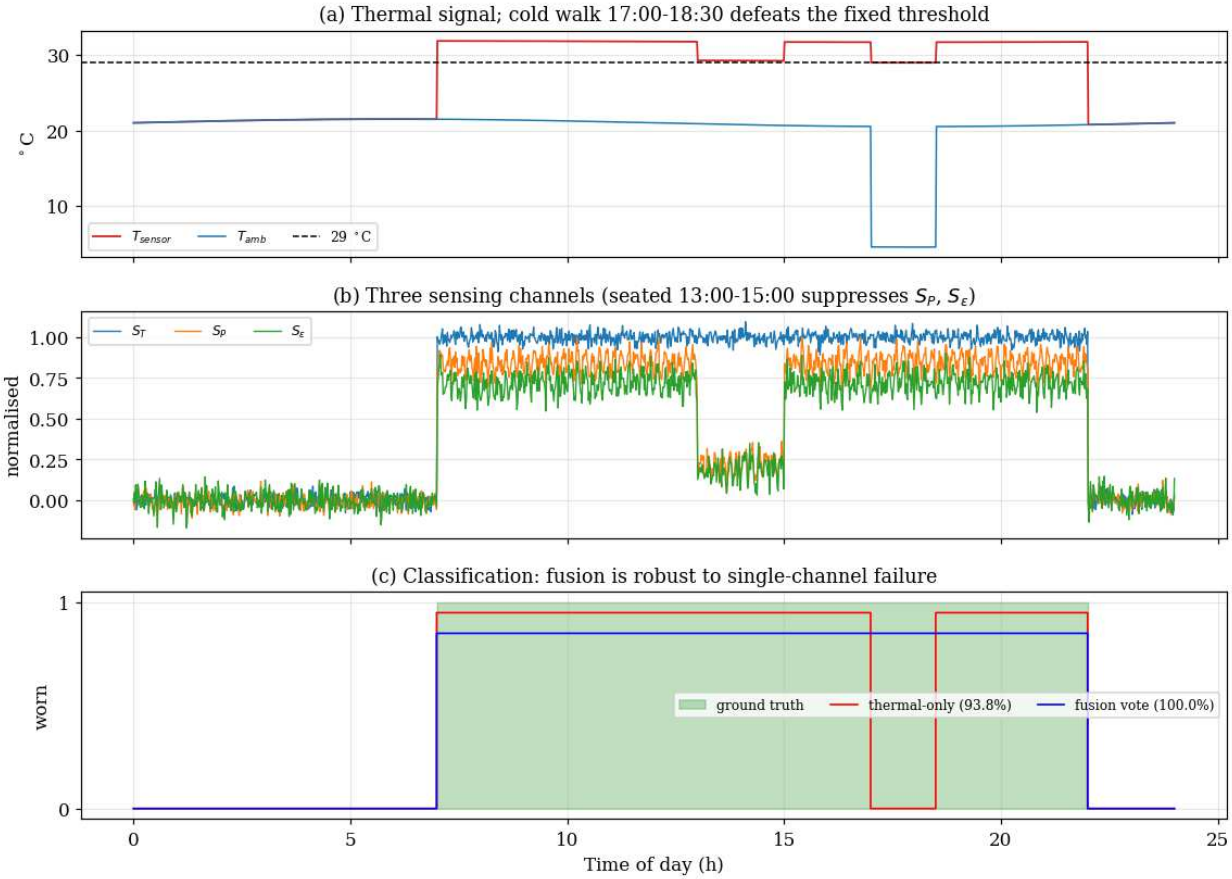


Figure 7: Multi-modal fusion over a synthetic 24-hour wearing day. (a) The sensor and ambient temperatures produced by the thermal model of Section 3; the cold outdoor walk from 17:00 to 18:30 drives the sensor reading below the fixed 29 °C threshold despite continuous wear. (b) The three normalised sensing channels; the sedentary seated period from 13:00 to 15:00 suppresses the pressure and strain channels while the thermal channel persists. (c) Classification outcomes: the thermal-only fixed-threshold classifier (red, 93.8 % accuracy) fails during the cold interval, whereas the weighted fusion vote of Eq. (15) (blue, 100 % accuracy) remains correct throughout, illustrating robustness against single-channel failure.

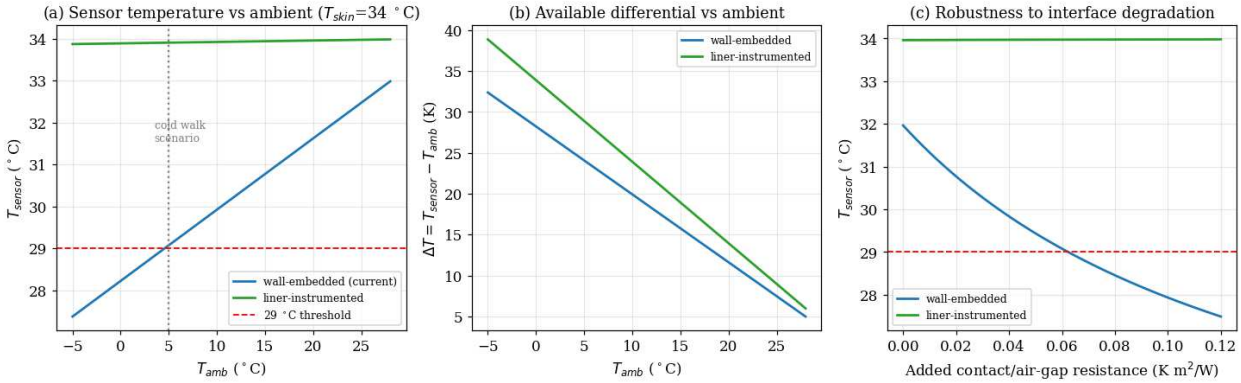


Figure 8: Sensor placement analysis: instrumenting the liner versus the socket wall. (a) Sensor temperature versus ambient temperature for a wall-embedded sensor (blue, the geometry of Section 3) and a 0.1 mm liner-side film at the residual limb–liner interface (green), at $T_{\text{skin}} = 34\,^{\circ}\text{C}$; the liner-side sensor tracks skin temperature and remains far above the 29 °C threshold even at the 5 °C cold-walk ambient. (b) The temperature differential available to each placement. (c) Robustness to contact and air-gap degradation at the liner–socket interface: added resistance drives the wall-embedded sensor below threshold but lies on the exterior side of the liner-side sensor and slightly raises its reading.

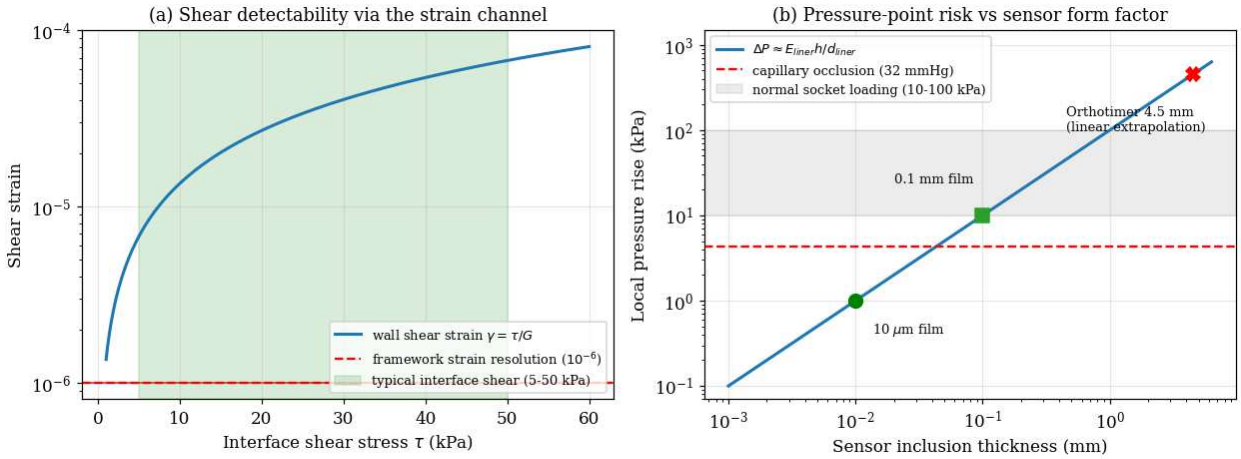


Figure 9: Interface mechanics of the sensorised socket. (a) Shear detectability via the strain channel: interface shear stresses in the typical 5 kPa to 50 kPa range (shaded) produce PETG wall shear strains of 7×10^{-6} to 7×10^{-5}, one to two orders of magnitude above the framework's predicted 10^{-6} strain resolution (dashed) [15]. (b) Pressure-point risk versus sensor form factor: the first-order local pressure rise $\Delta P \approx E_{\text{liner}} h / d_{\text{liner}}$ for an inclusion of thickness h at the residual limb–liner interface, with the capillary occlusion pressure (32 mmHg, dashed) and the normal socket loading range (shaded) marked. A 10 µm film remains sub-capillary; the 4.5 mm Orthotimer housing lies far beyond the linear regime and is plotted at the linear extrapolation for reference only. Both panels are generated by the open verification notebook.